

AAAAAAA

A DISSERTATION PRESENTED
BY
FRANCESCO IOLI
TO
THE DEPARTMENT OF PSYCHOLOGY

IN PARTIAL FULFILLMENT OF THE REQUIREMENTS
FOR THE DEGREE OF
DOCTOR OF PHILOSOPHY
IN THE SUBJECT OF
PSYCHOLOGY

HARVARD UNIVERSITY
CAMBRIDGE, MASSACHUSETTS
MAY 2024

©2023 – FRANCESCO IOLI

ALL RIGHTS RESERVED.

AAAAAAA

ABSTRACT

Lorem ipsum dolor sit amet, consectetuer adipiscing elit. Morbi commodo, ipsum sed pharetra gravida, orci magna rhoncus neque, id pulvinar odio lorem non turpis. Nullam sit amet enim. Suspendisse id velit vitae ligula volutpat condimentum. Aliquam erat volutpat. Sed quis velit. Nulla facilisi. Nulla libero. Vivamus pharetra posuere sapien. Nam consectetuer. Sed aliquam, nunc eget euismod ullamcorper, lectus nunc ullamcorper orci, fermentum bibendum enim nibh eget ipsum. Donec porttitor ligula eu dolor. Maecenas vitae nulla consequat libero cursus venenatis. Nam magna enim, accumsan eu, blandit sed, blandit a, eros.

Quisque facilisis erat a dui. Nam malesuada ornare dolor. Cras gravida, diam sit amet rhoncus ornare, erat elit consectetuer erat, id egestas pede nibh eget odio. Proin tincidunt, velit vel porta elementum, magna diam molestie sapien, non aliquet massa pede eu diam. Aliquam iaculis. Fusce et ipsum et nulla tristique facilisis. Donec eget sem sit amet ligula viverra gravida. Etiam vehicula urna vel turpis. Suspendisse sagittis ante a urna. Morbi a est quis orci consequat rutrum. Nullam egestas feugiat felis. Integer adipiscing semper ligula. Nunc molestie, nisl sit amet cursus convallis, sapien lectus pretium metus, vitae pretium enim wisi id lectus. Donec vestibulum. Etiam vel nibh. Nulla facilisi. Mauris pharetra. Donec augue. Fusce ultrices, neque id dignissim ultrices, tellus mauris dictum elit, vel lacinia enim metus eu nunc.

Contents

1	INTRODUCTION	1
1.1	Motivation and relevance	2
1.2	The Belvedere Glacier	2
	References	4
2	BACK TO THE PAST: RECONSTRUCTING GLACIER GEOMETRY WITH HISTORICAL AERIAL IMAGES (1977-2009)	5
2.1	Introduction	6
2.2	Datasets	6
2.3	Methods	6
2.4	Discussion	6
2.5	References	6
	References	7
3	UAV PHOTGRAMMETRY FOR ANNUAL GLACIER RECONSTRUCTION (2015-2023)	8
3.1	Introduction	9
3.2	Instruments and datasets	9
3.3	Methodology	II
3.4	Results	13
3.5	Discussion	19
	References	20
4	DEEP LEARNING LOW-COST PHOTGRAMMETRY FOR 4D SHORT-TERM GLACIER MONITORING (2022-2023)	21
4.1	Introduction	22
4.2	The low-cost stereoscopic system	22
4.3	Datasets	31
4.4	Methodology	33
	References	35
5	RESULTS	36

6	DISCUSSION	37
7	CONCLUSION	38
	APPENDIX A SOME EXTRA STUFF	39

Listing of figures

1.1	(a) Location of Belvedere Glacier, base map (source: Swisstopo www.geo.admin.ch); (b) Picture of ...	2
3.1	(a) An example of a photogrammetric target deployed over the glacier moraine; (b) location of the targets used for the photogrammetric surveys. For each year, a subset of the targets were used as GCPs, while the remaining as CPs.	12
3.2	Barplot of reprojection RMSE computed CPs for each photogrammetric model. Due to practical problems occurred in 2020 and explained in Section 3.4.5, the RMSE of 2020 model was split in two parts: <i>2020 lower</i> denotes the CP RMSE over related to the central and lower sectors of the glacier (S_2 and S_3 in Figure ??a), whereas <i>2020 upper</i> refers to the upper accumulation sector only (S_1).	14
3.3	Orthophotos obtained from the photogrammetric model for each year. (a) 2015, (b) 2016, (c) 2017, (d) 2018, (e) 2019, (f) 2020, (g) 2021, (h) 2022, (i) 2023.	15
3.4	Yearly volume variation computed as difference between DSM of two consecutive years. The error bars plotted represent the uncertainty of each estimated value. Note that the values on the Y axis are expressed in million of m^3 .	16
4.1	(a) Map of the Belvedere Glacier, with marked the location of the two cameras C1 and C2, the Automatic Weather Station (AWS) and the Zamboni Zappa Hut; (b) The area of study: the stereoscopic reconstruction is focused on the terminal ice cliff (dashed light blue line), while the monoscopic DIC processing from camera C2 image sequence is focused on the upper area of the north lobe (dashed green line).	22
4.2	Scheme of the proposed acquisition system configuration for a single monitoring station. Arrows indicate the direction of signal initiation. Image adapted from Greig Sheridan's repository.	24
4.3	Stripboard on which are soldered the main components of the internal circuit: capacitors (1), voltage regulators (2), real-time clock with coin-cell battery (3), Arduino Pro Mini (4), optoisolators (5), and Raspberry Pi Zero W (6).	26
4.4	Example of some of the pages of the web-based interface to remotely control the monitoring units.	27

4.5	Battery voltage and temperature of boards with and without the solar panel during a period of tests. Starting from a fully charged condition, the system was kept without solar panel at around 2 °C for the first six days. After nine days, the battery was fully discharged and the system was reconnected to the panel and exposed to solar radiation.	29
4.6	(a) Picture of the monitoring unit prototype installed for tests at the Belvedere Glacier site. (b) Picture of the final monumentation of the camera installed on the stream-wise right moraine. TODO: change picture with the final installation	30
4.7	(a) UAV-A block and (b) UAV-B block processed with Agisoft Metashape. The flags represent the targets used either as GCPs in the BA or as CPs to evaluate the quality of the photogrammetric block.	32
4.8	General workflow with two parallel processing chains involving stereoscopic reconstruction of terminal ice cliff from stereo-pairs of images to derive ice volume losses at the glacier terminus and glacier retreat and monoscopic digital-image correlation to derive surface velocities. 34	

Acknowledgments

LOREM IPSUM DOLOR SIT AMET, consectetur adipiscing elit. Morbi commodo, ipsum sed pharetra gravida, orci magna rhoncus neque, id pulvinar odio lorem non turpis. Nullam sit amet enim. Suspendisse id velit vitae ligula volutpat condimentum. Aliquam erat volutpat. Sed quis velit. Nulla facilisi. Nulla libero. Vivamus pharetra posuere sapien. Nam consectetur. Sed aliquam, nunc eget euismod ullamcorper, lectus nunc ullamcorper orci, fermentum bibendum enim nibh eget ipsum. Donec porttitor ligula eu dolor. Maecenas vitae nulla consequat libero cursus venenatis. Nam magna enim, accumsan eu, blandit sed, blandit a, eros.

1

Introduction

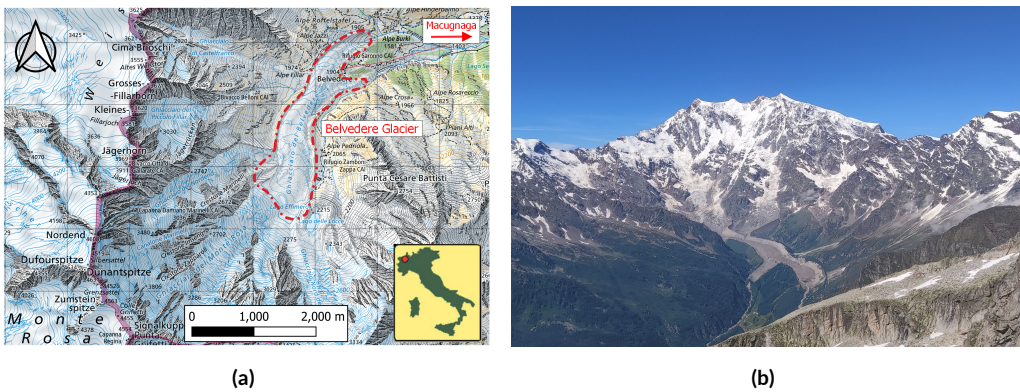


Figure 1.1: (a) Location of Belvedere Glacier, base map (source: Swisstopo www.geo.admin.ch); (b) Picture of ...

1.1 MOTIVATION AND RELEVANCE

1.2 THE BELVEDERE GLACIER

The Belvedere Glacier (Randolph Glacier Inventory code RGI60-11.02858) is an alpine glacier in Valle Anzasca (Italy), on the east side of the Monte Rosa Massif ($N\ 45^{\circ}58' E\ 7^{\circ}55'$) (Fig. 1.1). The lower part of the Belvedere Glacier is a temperate debris-covered glacier, that covers an area of $\sim 1.8\ km^2$ and extends from an altitude of $\sim 2250\ m\ a.s.l.$ to $\sim 1800\ m\ a.s.l.$. This region is characterized by a gentle slope, and it is fed by ice falls and snow avalanches coming from the Monte Rosa East Face (Haeberli et al., 2002). In its low-relief sector, the Belvedere Glacier splits into two lobes, reaching $\sim 1800\ m\ a.s.l.$. The northern lobe, in particular, ends with a prominent ice cliff, from which the River Anza springs.

Similarly to Miage glacier (Monte Bianco, Valle d'Aosta), the Belvedere Glacier is almost completely covered by rocks and boulders with dimensions ranging from few decimetres to some meters, which makes it a *black glacier*. Due to the global warming trend, the number of black glaciers along the Italian Alps is rising (Diolaiuti et al., 2003). Up to the beginning of the century, the debris cover helped to compensate the effect of the increased temperature, establishing a negative feedback in the temperature-ablation relationship (Roethlisberger et al., 1985, Diolaiuti et al., 2003). However, in recent years, the debris cover protection has not been sufficient to limit the glacier retreat.

In the past, several hazardous events originated by the Belvedere Glacier, such as floods and slope instability, threatened the nearby village of Macugnaga and the Zamboni Zappa Hut, at 2070 m a.s.l. (Kääb et al., 2004). At the beginning of the 21st century, the Belvedere Glacier was characterized by a particular surge-type dynamics (Haeberli et al., 2002). During the late 1990s, the surface speeds of the whole glacier were ranging

between 30 m y^{-1} and 45 m y^{-1} (Roethlisberger et al., 1985, Kääb et al., 2005). During 2000–2001 an accelerated flow in the Monte-Rosa Glacier produced a wave of compression-decompression stresses and strains in the Belvedere Glacier. Surface velocities soared: values up to 200 m y^{-1} were observed photogrammetrically during autumn 2001 (Kääb et al., 2004). The ice thickness increased more than 20 m and the wave travelled downwards, creating a depression area in the accumulation zone, that was filled by a super-glacial lake, the Lago Effimero (Haeberli et al., 2002, Mortara et al., 2009).

References

- Diolaiuti, G., D'Agata, C., & Smiraglia, C. (2003). Belvedere Glacier, Monte Rosa, Italian Alps: Tongue Thickness and Volume Variations in the Second Half of the 20th Century. *Arctic, Antarctic, and Alpine Research*, 35(2), 255–263.
- Haeberli, W., Kääb, A., Paul, F., Chiarle, M., Mortara, G., Mazza, A., Deline, P., & Richardson, S. (2002). A surge-type movement at Ghiacciaio del Belvedere and a developing slope instability in the east face of Monte Rosa, Macugnaga, Italian Alps. *Norsk Geografisk Tidsskrift*, 56(2), 104–111.
- Kääb, A., Huggel, C., Barbero, S., Chiarle, M., Cordola, M., Epifani, F., & Haeberli, W. (2004). Glacier Hazards At Belvedere Glacier and the Monte Rosa East Face , Italian Alps: Processes and Mitigation. *Internationales Symposium INTERPRAEVENT 2004 – RIVA / TRIENT*, (Vc), 67–78.
- Kääb, A., Huggel, C., Fischer, L., Guex, S., Paul, F., Roer, I., Salzmann, N., Schlaefli, S., Schmutz, K., Schneider, D., Strozzi, T., & Weidmann, Y. (2005). Remote sensing of glacier-and permafrost-related hazards in high mountains: an overview. *Natural Hazards and Earth System Science*, 5(4), 527–554.
- Mortara, G., Tamburini, A., Ercole, G., Semino, P., Chiarle, M., Godone, F., Giuliano, M., Haeberli, W., Kääb, A., Huggel, C., Fischer, L., Cordola, M., Barbero, S., Salandin, A., Rabuffetti, D., Mercalli, L., Berro, D. C., Carton, A., Mazza, A., Godone, D., Federici, P., Viazza, G., Epifani, F., & Valsesia, T. (2009). *Il ghiacciaio del Belvedere e l'emergenza del Lago Effimero. Regione Piemonte*. Societa' Meteorologica Subalpina.
- Roethlisberger, H., Haeberli, W., Schmid, W., Biolzi, M., & Pika, J. (1985). Studi Sul Comportamento Del Ghiacciaio Del Belvedere. *Comunità montana della Valle Anzasca*, (97.3).

2

Back to the past: reconstructing glacier geometry with historical aerial images (1977-2009)

THIS CHAPTER IS BASED ON:

De Gaetani, C. I., Ioli, F., & Pinto, L. (2021). Aerial and UAV Images for Photogrammetric Analysis of Belvedere Glacier Evolution in the Period 1977–2019. *Remote Sensing*, 13(18), 3787. <https://doi.org/10.3390/rs13183787>

2.1 INTRODUCTION

2.2 DATASETS

2.2.1 HISTORICAL AERIAL DATASETS OF 1977, 1991 AND 2001

2.2.2 DIGITAL AERIAL AND UAV DATASETS OF 2009 AND 2019

2.2.3 GNSS SURVEY FOR BLOCK GEOREFERENCING

2.3 METHODS

2.4 DISCUSSION

2.5 REFERENCES

References

3

UAV photogrammetry for annual glacier reconstruction (2015-2023)

THIS CHAPTER IS BASED ON:

Ioli, F., Bianchi, A., Cina, A., De Michele, C., Maschio, P., Passoni, D., & Pinto, L. (2021). Mid-Term Monitoring of Glacier's Variations with UAVs: The Example of the Belvedere Glacier. *Remote Sensing*, 14(1), 28.
<https://doi.org/10.3390/rs14010028>

3.1 INTRODUCTION

3.2 INSTRUMENTS AND DATASETS

Short intro to section...

3.2.1 UAV FLIGHTS

Because of the long duration of the monitoring campaign, the challenging environment and the fact that more than one research group was involved in the project, different UAV platforms and cameras were used. As reported in Table 3.1, in 2015 and 2016, a ready-to-fly fixed-wing UAV SenseFly eBee, equipped with a compact camera Canon PowerShot S110, was employed to survey the whole glacier. During 2017, different combinations of UAVs (fixed-wing and quadcopters) and cameras were employed (Table 3.1). From 2018 to 2020, a low-cost recreational fixed-wing UAV Parrot Disco FPV, with a wingspan of 1.15 m and a weight of 750 g, was adapted to carry a small and lightweight action cam Hawkeye Firefly 8S. For each camera, the main sensor and objective characteristics are listed Table 3.2.

UAVs flights were conducted automatically by using ground station software packages developed by UAV manufacturers. [Add UGCS...](#)

The flights were designed to have GSD ranging between 5 cm and 10 cm, and to guarantee ~80 % of longitudinal and ~60 % of transversal overlap. Average image GSD values and number of GCPs and CPs, used respectively to orient the images and to assess the quality of the photogrammetric blocks, are summarized in Table 3.1.

[Add instruments for 2021-2023...](#)

3.2.2 GNSS MEASUREMENTS

A set of GCPs was materialized with square cross targets, printed on polypropylene sheets and anchored on big rocks (Figure 3.1b). About 25 targets were deployed over the glacier (named hereafter as *moving targets* or *M#* in Figure 3.1a) and 24 targets (labelled as *stable targets* or *S#* in Figure 3.1a) were placed on stable areas along the moraines so that they were not subjected neither to the ice flow nor to rock falls. Every year, the condition of each target was checked and, if one was damaged or destroyed, the polypropylene sheet was replaced by keeping the same location of the center (i.e., by using the same fisher plugs). During the years, some targets were lost, and therefore new ones were materialized (e.g., M29bis). Targets were yearly surveyed with dual frequency (L1/L2) geodetic quality GNSS receivers and their coordinates were framed within the official Italian reference

Table 3.1: Summary of the characteristics of the surveys.

Year	Date	UAV	Camera	GSD [m/px]	GCP [#]	CP [#]
2015	A. 8.10 B. 23.10	SenseFly eBee	Canon PowerShot S110	0.07	24	11
2016	20.10	SenseFly eBee	Canon PowerShot S110	0.09	31	15
2017	A. 5.10 B. 15.11 C. 16.11	A. SenseFly eBee B. SenseFly eBee Plus C. DJI Phantom 4 Pro	A. Canon PowerShot S110 B. SenseFly S.O.D.A C. DJI FC6310	0.06	27	8
2018	23-25.07	Parrot Disco	Hawkeye Firefly 8S	0.05	27	13
2019	29.07- 2.08	Parrot Disco	Hawkeye Firefly 8S	0.06	26	10
2020	A. 26- 27.07 B. 9.08	A. Parrot Disco B. DJI Phantom 4 Pro	A. Hawkeye Firefly 8S B. DJI FC6310	0.05	29	12

Table 3.2: Summary of the characteristics of the cameras employed.

Camera	Sensor	Sensor Size [mm ²]	Focal length [mm]	Image size [px]	Pixel size [μm]
Canon PowerShot S110	1/1.7" CMOS	7.44 × 5.58	5.2	4000 × 3000	1.9
SenseFly S.O.D.A	1" CCD	13.2 × 8.8	10.6	5472 × 3648	2.4
DJI FC6310	1" CMOS	13.2 × 8.8	8.8	5472 × 3648	2.4
Hawkeye Firefly 8S	1/2.3" CMOS	6.17 × 4.56	3.8	5472 × 3648	1.34

system ETRF2000 at the epoch 2008.0, projected in UTM 32N. For the lower part of the glacier, where the GSM network connection was available, target position was obtained in nRTK with respect to a network of CORS permanent stations (either HxGN SmartNet or SPIN GNSS). The points were occupied at least twice, each time for a duration of 5 s. By contrast, in the upper part of the glacier, targets were surveyed with static sessions of \sim 10 min, and raw observation data was post-processed with respect to local master stations, located on stable and well known points. To this end, either the point S_{12} , placed on a big rock next to the Zamboni-Zappa hut, or the point S_{20} , located near the Rifugio Ghiacciai del Rosa on the Belvedere hill, were used (see Figure 3.1a). Accuracy of GNSS measurements was evaluated empirically by comparing repeated measurements over stable targets carried out in different years. RMSE of 1.5 cm in planimetry and 3 cm in elevation were obtained.

3.3 METODOLOGY

3.3.1 SfM WORKFLOW

In order to build photogrammetric models of the glacier, images acquired during UAV surveys were processed with the SfM software Agisoft Metashape 1.7.2 ([Agisoft, 2023](#)). For each year, at least 24 GCPs spread over the glacier were employed to orient the images, whereas at least 10 Check Points (CPs) were used to assess models quality. Both GCPs and CPs were manually collimated on the images. Tie Points (TPs) were detected and matched by Metashape on full resolution images (which corresponds to *high accuracy* parameter in Metashape). Image External Orientation (EO) and TPs world coordinates were estimated by solving the Bundle Block Adjustment (BBA). TPs with the worst reprojection error on images, which are likely originated from false matches, were removed and the BBA was solved again to improve quality of BBA solution. This process was iterated more times until TPs mean reprojection error had dropped below 0.7-0.8 px. Camera internal orientation was estimated by self-calibration (?), because of its instability in the cameras employed.

Dense 3D reconstruction was computed by Agisoft Metashape with proprietary MVS algorithms (?). Depth maps and dense point clouds were obtained from images downsampled by a factor 4, in order to reduce the computational time (*medium quality* parameter of the dense cloud generation in Metashape). Triangulated mesh surfaces and photorealistic textures were computed.

DSMs with a resolution of 0.5 m px^{-1} were derived from the mesh model. Finally, orthophotos with a GSD of 0.10 m px^{-1} were obtained by projecting the most nadiral images over the mesh model (Figure 3.3).

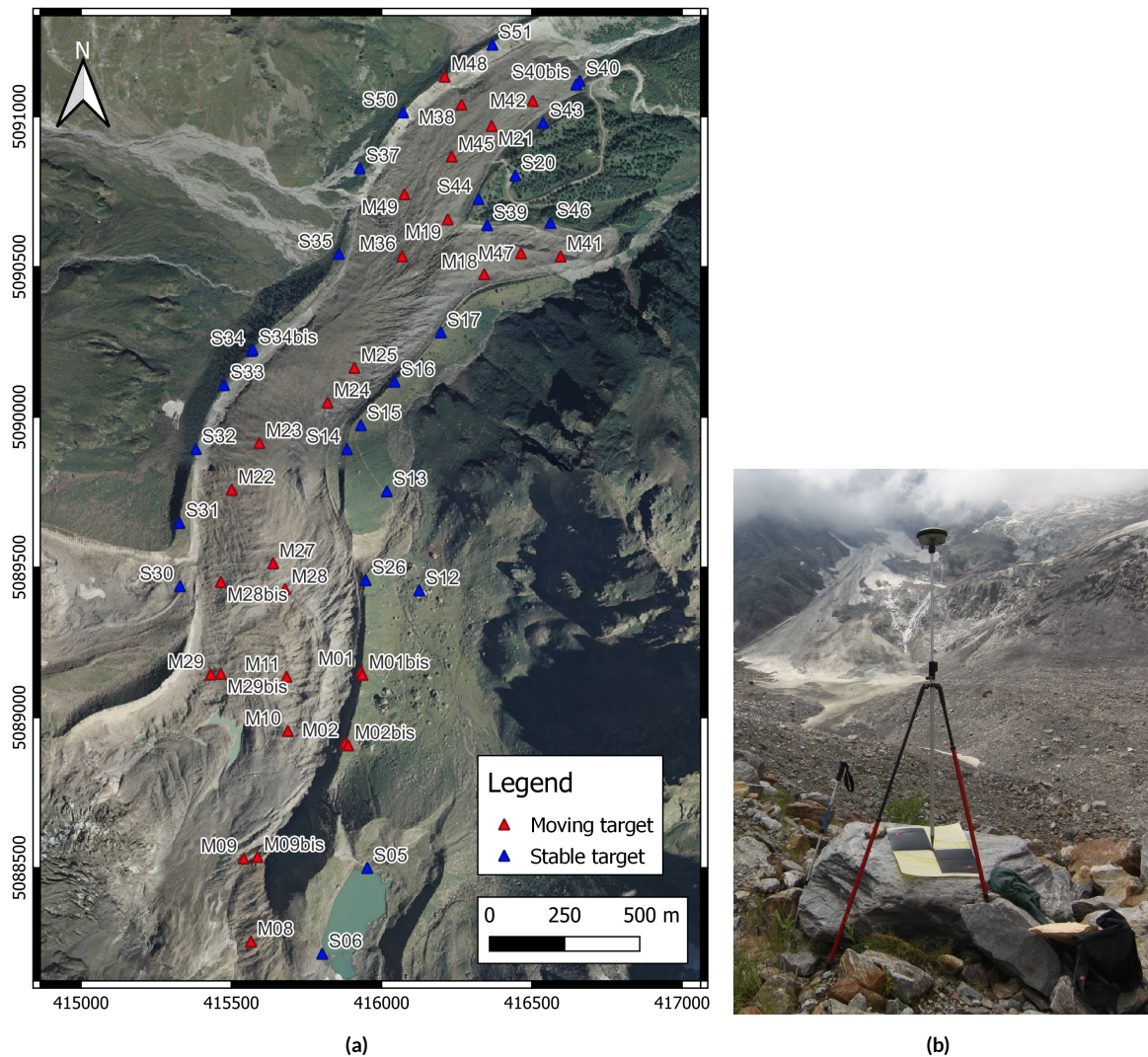


Figure 3.1: (a) An example of a photogrammetric target deployed over the glacier moraine; (b) location of the targets used for the photogrammetric surveys. For each year, a subset of the targets were used as GCPs, while the remaining as CPs.

3.3.2 GLACIER FLOW VELOCITY

3.3.3 VOLUME VARIATIONS

To compute glacier volume variation ΔV , consecutive DSMs were differentiated by employing a DEM of Difference (DOD) approach with the tool *Compute 2.5D volume* implemented in CloudCompare ?. First, photogrammetric dense clouds were gridded by projecting points along the vertical direction on a planar surface, obtaining DSMs with a cell footprint on ground of 0.5 m \times 0.5 m. The choice of the raster resolution was a compromise to achieve a robust height field estimation by averaging a large enough number of points for each cell of the raster, but at the same time small enough to maintain a spatial resolution able to map small scale glacier morphology. A mask was manually created and applied to all the DSMs to exclude areas outside the glacier surface. DSMs from consecutive years were then differentiated pixel-by-pixel to obtain the height difference at each cell of the raster.

3.4 RESULTS

3.4.1 SFM

The re-projection RMSE over the CPs are shown in Figure 3.2 as assessment of the geometrical accuracy of the models. The global re-projection RMSE was mostly ranging between 0.1 m and 0.2 m. The only exception consisted in the upper sector (comparable to sector S1 in Figure ??a) of the 2020 model, for which the RMSE is almost double compared to the other values. This was caused by practical problems occurred in 2020, explained in detail in Section 3.4.5. As a consequence, the value of 2020 RMSE was split in two different bars in the graph. From 2015 to 2017, when compact cameras were used, errors comparable to 1.5 times the GSD were obtained. Since 2018, a lightweight action-cam has been employed to minimize the UAV take-off weight and this has led to an RMSE up to 3 times the GSD, but still always smaller than 0.2 m.

3.4.2 GLACIER FLOW VELOCITY

3.4.3 VOLUME VARIATIONS

Add 2021-2023!

In order to rigorously estimate volume variation variances, by propagating the variance, it would be necessary to know the covariance matrix of each DSM, considered as a multivariate random variable with dimension equal to the number of cells. However, no information concerning cells covariances was provided by

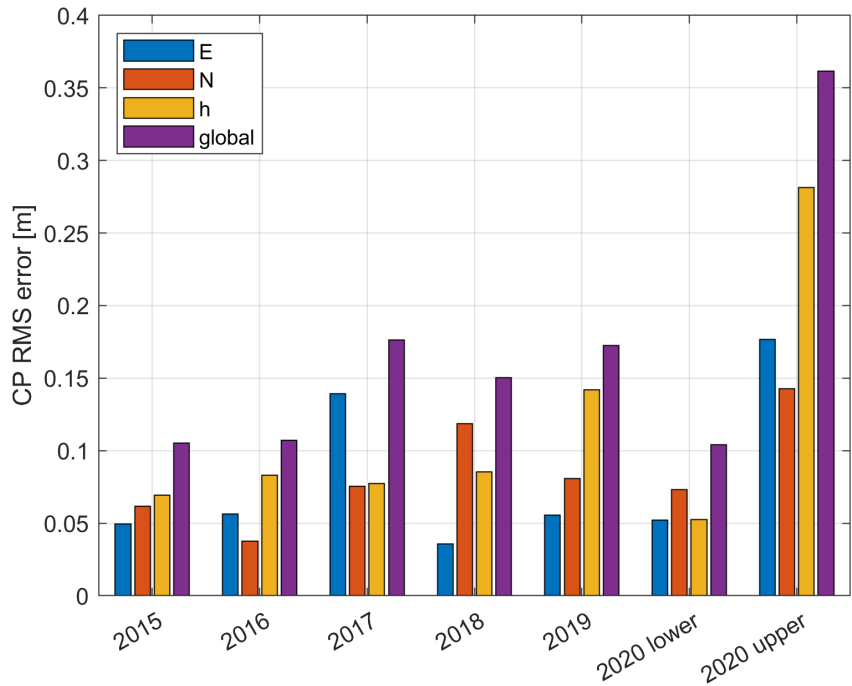


Figure 3.2: Barplot of reprojection RMSE computed CPs for each photogrammetric model. Due to practical problems occurred in 2020 and explained in Section 3.4.5, the RMSE of 2020 model was split in two parts: 2020 lower denotes the CP RMSE over related to the central and lower sectors of the glacier (S2 and S3 in Figure ??a), whereas 2020 upper refers to the upper accumulation sector only (S1).

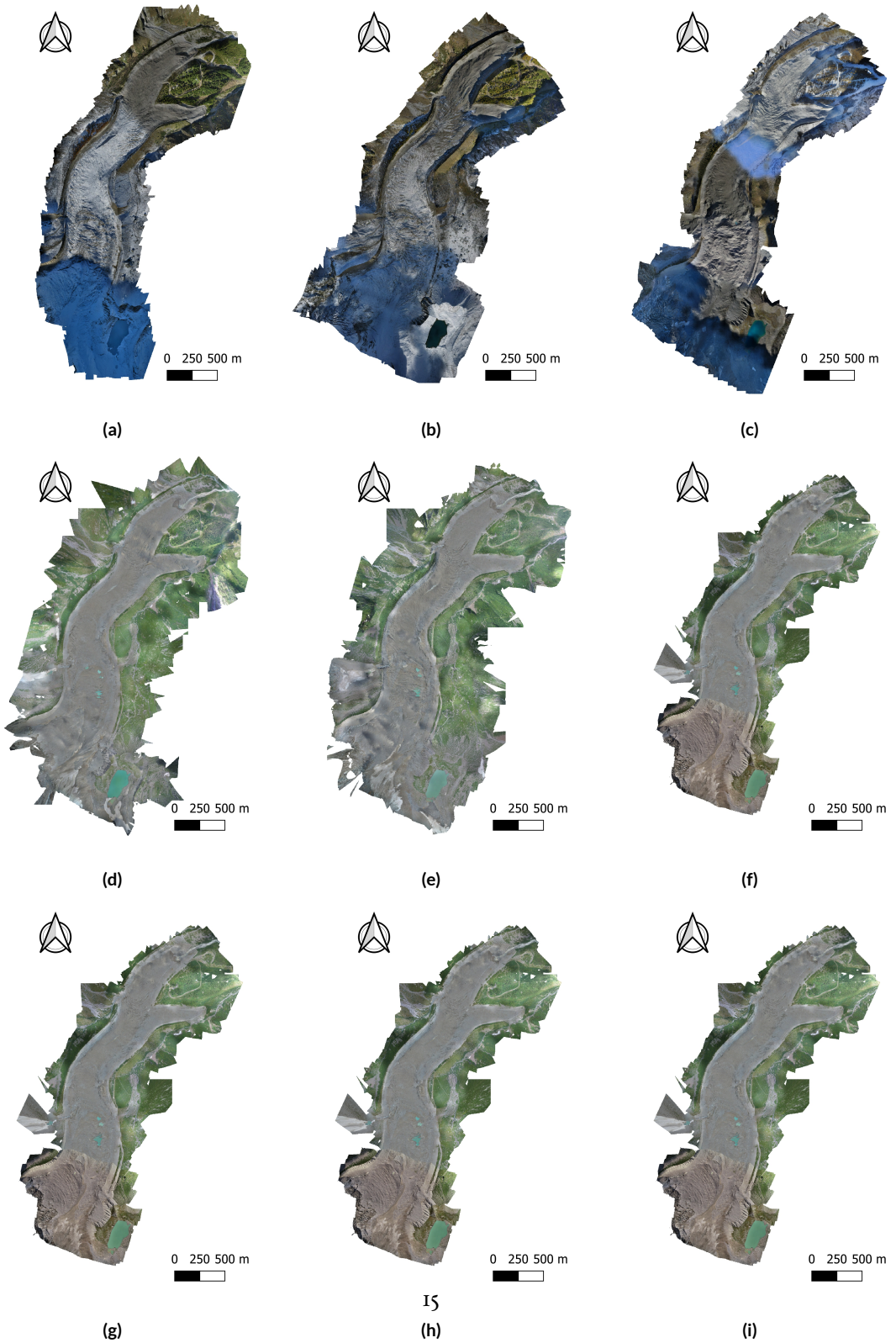


Figure 3.3: Orthophotos obtained from the photogrammetric model for each year. (a) 2015, (b) 2016, (c) 2017, (d) 2018, (e) 2019, (f) 2020, (g) 2021, (h) 2022, (i) 2023.

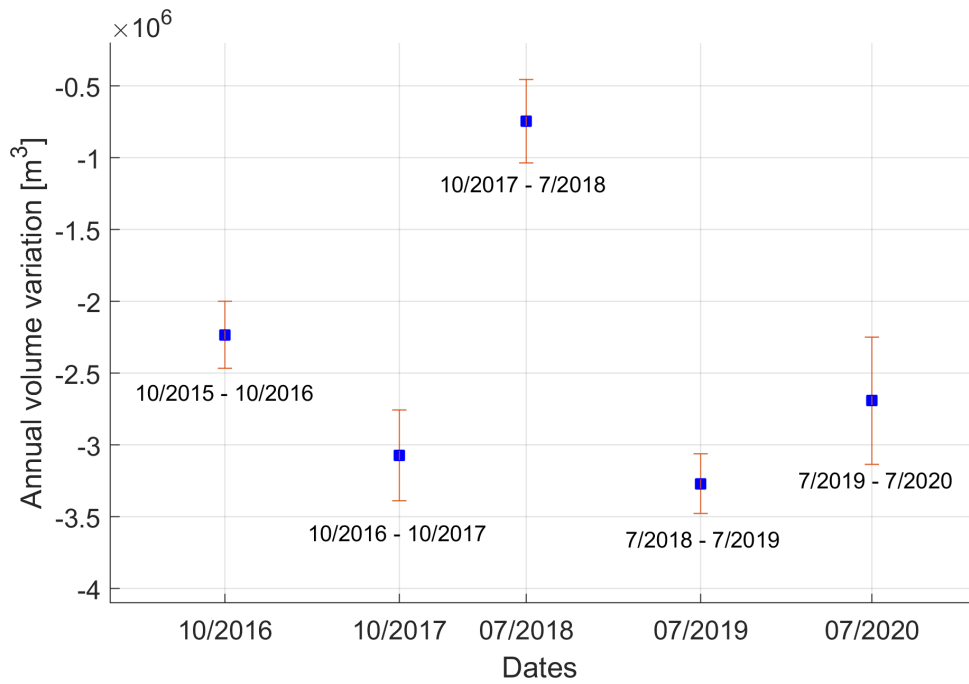


Figure 3.4: Yearly volume variation computed as difference between DSM of two consecutive years. The error bars plotted represent the uncertainty of each estimated value. Note that the values on the Y axis are expressed in million of m³.

the SfM software employed, thus it was troublesome to compute covariances between nearby cells in a DSM (which are clearly correlated because they were generated by the same set of images in the photogrammetric process). As a consequence, only a rough estimation of the variance was carried out by considering each DSM as a mono-dimensional random variable with variance equal to the squared value of the vertical component of RMSE computed on the CPs of the relative photogrammetric model (see Figure 3.2). Moreover, $DSM^{(i+1)}$ and $DSM^{(i)}$ were considered as independent because there was no relation between the surveys. The variance of the volume variation was therefore computed as:

$$\sigma_{\Delta V^{(i+1,i)}}^2 = (n \times A_c)^2 (\sigma_{DSM^{(i+1)}}^2 + \sigma_{DSM^{(i)}}^2), \quad (3.1)$$

where n is the number of cell in the DSMs and σ_{DSM}^2 is the squared vertical error of the photogrammetric model evaluated on the GCPs.

For the years 2015–2016, 2016–2017, 2017–2018, the glacier was partially covered by snow (see Figure 3.3a–c), which introduced additional uncertainties in volume estimation. The snow height accumulated at the nivometric station located near Zamboni Zappa Hut (2075 m a.s.l., in the central sector of the glacier) on the survey dates was retrieved from the meteorological database of ARPA Piemonte, the regional agency for the environment ?: 22 cm of snow were measured on 23 October 2015, 20 cm on 20 October 2016, 40 cm on 15 November 2017. The measured snow heights were considered as additional components of DSM standard deviations. Yet, because the glacier was only partially covered by snow, the snow-driven uncertainty was weighted by half of the total glacier area in variance propagation. Figure 3.4 illustrates the loss of ice volume year by year. The estimated variance of the glacier volume variation is plotted as an error bar for each value of volume variation.

Between 2017 and 2018, fieldworks were moved from Autumn to Summer. Therefore, the loss of volume for the year 2017–2018 was computed between October 2017 and July 2018, therefore it represented only the variation occurred in wintertime and springtime, and it should not be directly compared with the annual average. Indeed, 2017–2018 volume variation was $-0.75 \times 10^6 \text{ m}^3$, against the average variation between 2015 and 2020 of $-2.81 \times 10^6 \text{ m}^3$ (difference of 27 %). Ice volume loss for the year 2019–2020 may be slightly underestimated as well: the photogrammetric model of the upper part of the glacier was affected by a larger geometric (RMSE in vertical direction of = 0.28 m, see Section 3.4.5) compared to the others models, due to the lack of GCPs measured in-situ at the time of the photo acquisition. Overall, the negative ice volume variation occurred between 2015 and 2020 is evident and significant: every year, between $2 \times 10^6 \text{ m}^3$ and $3.5 \times 10^6 \text{ m}^3$ of ice were lost.

3.4.4 GLACIER OUTLINE

3.4.5 PROBLEMS ARISING DURING THE SURVEYS OF 2017 AND 2020

Conducting a yearly monitoring campaign in an alpine environment for six consecutive years is challenging because of, for example, the hard accessibility of some areas of the glacier (also for fixed-wing UAVs take-off and landing) and the variability of the meteorological conditions.

Adverse meteorological conditions and practical issues made it necessary to split the 2017 survey in different dates, and various UAVs and cameras were employed (see Table 3.1). The 2017 photogrammetric model was therefore divided into three parts: the central part refers to the October survey while the lower and the upper parts refer to the November survey and at that time the glacier was covered by snow (Figure 3.3c). Technical problems arose also during the 2020 survey: a breakage of one elevon servo during a landing phase caused the fixed-wing UAV to crash. Therefore, a quadcopter DJI Phantom 4 Pro was employed to survey the upper part of the glacier (approximately the S1 sector, see the different colors in the orthophoto of Figure 3.3f) 14 days after the former. However, during the August 2020 fieldwork, it was not possible to measure any additional GCPs because the south-west part of the Belvedere Glacier, close to the Monte-Rosa Glacier is hardly accessible and dangerous due to the presence of crevasses and steep rocks. The few GCPs available in the upper part of the glacier made necessary to co-register the Phantom 4 Pro model on the 2019 model, by searching for sharp edges of rocks along the moraines, remained fixed along the year, on 2019 images. This approach is less accurate than measuring targets directly on the field. The RMSE on CPs was therefore equal to 0.36 m (see Figure 3.2), ~ 7 times the GSD. Nevertheless, the area affected by this issue was rather limited, compared to the whole Belvedere Glacier.

Moreover, between 2017 and 2018, the survey period was moved from Autumn to Summer. From 2015 to 2017, in fact, fieldworks were included within the DREAM project (see Section ??) and they took place in Autumn, at the beginning of the academic year. By contrast, from 2018 to 2020, surveys were carried out at the end of July because they were encompassed within a Summer School organized by DICA (Politecnico di Milano). The change in the survey dates was critical because the timespan occurred between the survey of October/November 2017 and that of July 2018 did not include the period of maximum ablation and velocity of the glacier (neither August 2017 nor August 2018). Therefore, volume variation and ice flow velocity refer mostly the wintertime and the results obtained are not directly comparable with those of the other years.

3.5 DISCUSSION

Several studies focused on understanding and quantifying Belvedere Glacier dynamics. Kääb et al. (2005) estimated velocities ranging between 32 m y^{-1} and 43 m y^{-1} on the whole Belvedere Glacier from October 1995 to September 1999, by employing aerial images. Besides, velocities between 100 m y^{-1} and 200 m y^{-1} were estimated by Kääb et al. (2005) in Autumn 2001, during the extraordinary surge event of 2000–2001. Nowadays, the Belvedere Glacier is clearly moving slower compared to the late 1990s. However, to the best of authors knowledge, there are no recent works estimating glacier flow velocities.

Concerning volume variations, Diolaiuti et al. (2003) digitalized two large-scale topographic maps to interpolate DSMs and estimate volume variations between 1957 and 1991. They found a positive volume difference of $+22.7 \times 10^6 \text{ m}^3$ (with an average rate of $\sim 0.69 \times 10^6 \text{ m}^3 \text{ y}^{-1}$, roughly assuming a linear volume variation during the years).

Their result matched with the study of Roethlisberger et al. (1985), who estimated an increase of the glacier height of $+1.5 \text{ m y}^{-1}$ between 1983 and 1985. Recently, De Gaetani et al. (2021) used historical aerial images and UAVs to photogrammetrically reconstruct glacier volume variations between 1977 and 2019. For the period 1977–1991, they confirmed the glacier expansion, with a volume increase of $+10.06 \times 10^6 \text{ m}^3$ ($+0.72 \times 10^6 \text{ m}^3 \text{ y}^{-1}$). The expansion continued up to 2001 (at the end of the surge event), with additional $10.61 \times 10^6 \text{ m}^3$ of ice gained. Since 2001, a severe glacier retreat has begun, with a loss of ice volume of $-47.78 \times 10^6 \text{ m}^3$ ($-5.97 \times 10^6 \text{ m}^3 \text{ y}^{-1}$) between 2001 and 2009. For the time-span 2009–2019, De Gaetani et al. (2021) derived a negative variation of $-27.16 \times 10^6 \text{ m}^3$ of ice ($-2.72 \times 10^6 \text{ m}^3 \text{ y}^{-1}$). This last ten-years-averaged estimate well matches with the annual volume variations found in this study between 2015 and 2020 (between $-2 \times 10^6 \text{ m}^3 \text{ y}^{-1}$ and $-3.5 \times 10^6 \text{ m}^3 \text{ y}^{-1}$).

References

Agisoft (2023). Metashape.

De Gaetani, C. I., Ioli, F., & Pinto, L. (2021). Aerial and UAV Images for Photogrammetric Analysis of Belvedere Glacier Evolution in the Period 1977–2019. *Remote Sensing* 2021, Vol. 13, Page 3787, 13(18), 3787.

Diolaiuti, G., D'Agata, C., & Smiraglia, C. (2003). Belvedere Glacier, Monte Rosa, Italian Alps: Tongue Thickness and Volume Variations in the Second Half of the 20th Century. *Arctic, Antarctic, and Alpine Research*, 35(2), 255–263.

Kääb, A., Huggel, C., Fischer, L., Guex, S., Paul, F., Roer, I., Salzmann, N., Schlaefli, S., Schmutz, K., Schneider, D., Strozzi, T., & Weidmann, Y. (2005). Remote sensing of glacier-and permafrost-related hazards in high mountains: an overview. *Natural Hazards and Earth System Science*, 5(4), 527–554.

Roethlisberger, H., Haeberli, W., Schmid, W., Biolzi, M., & Pika, J. (1985). Studi Sul Comportamento Del Ghiacciaio Del Belvedere. *Comunità montana della Valle Anzasca*, (97.3).

4

Deep learning low-cost photogrammetry for 4D short-term glacier monitoring (2022-2023)

THIS CHAPTER IS BASED ON:

- Paper under review on PFG
- Ioli, F., Bruno, E., Calzolari, D., Galbiati, M., Mannocchi, A., Manzoni, P., Martini, M., Bianchi, A., Cina, A., De Michele, C., and Pinto, L. (2023). A REPLICABLE OPEN-SOURCE MULTI-CAMERA SYSTEM FOR LOW-COST 4D GLACIER MONITORING, Int. Arch. Photogramm. Remote Sens. Spatial Inf. Sci., XLVIII-M-1-2023, 137-144,
<https://doi.org/10.5194/isprs-archives-XLVIII-M-1-2023-137-2023>

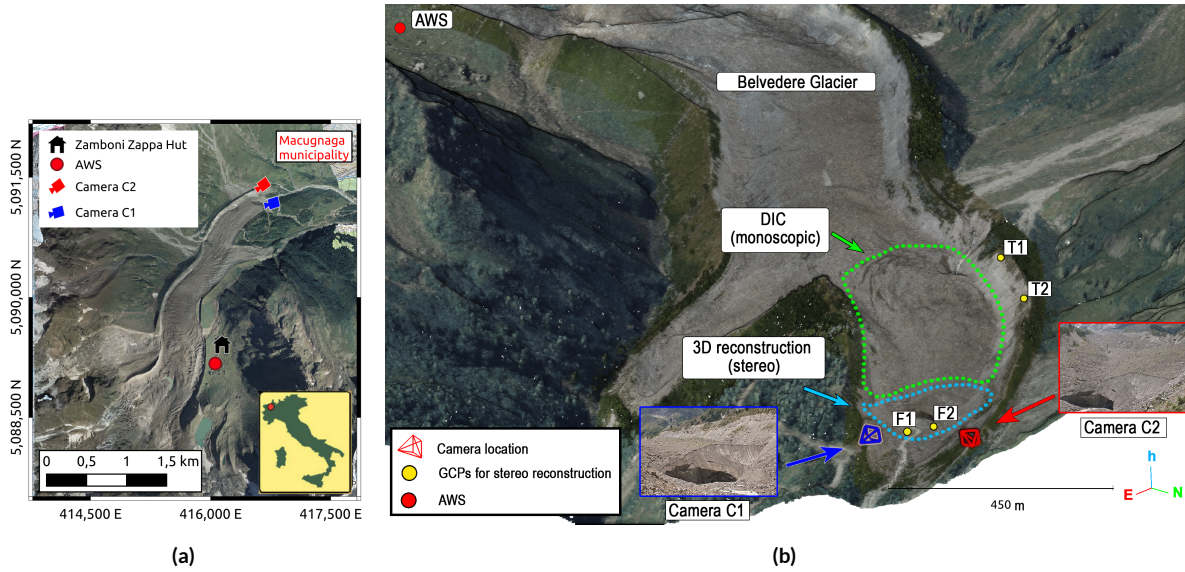


Figure 4.1: (a) Map of the Belvedere Glacier, with marked the location of the two cameras C1 and C2, the Automatic Weather Station (AWS) and the Zamboni Zappa Hut; (b) The area of study: the stereoscopic reconstruction is focused on the terminal ice cliff (dashed light blue line), while the monoscopic DIC processing from camera C2 image sequence is focused on the upper area of the north lobe (dashed green line).

4.1 INTRODUCTION

TODO: write introduction

4.2 THE LOW-COST STEREOSCOPIC SYSTEM

The low-cost stereoscopic system consists of two autonomous and independent monitoring units. Each unit is includes an off-the-shelf DSLR camera (Canon Eos 1200D), an Arduino microcontroller for camera triggering, and a Raspberry Pi Zero with a SIM card for sending images to a remote server via a GSM network(?). The instruments are housed in waterproof cases and mounted on tripods anchored to stable rocks along the glacier moraines. Power is supplied by a solar panel combined with a sealed lead-acid battery. The total cost of each unit was less than €2000, including camera and lens ?. The low-cost camera system is described in detail in ?.

The two monitoring stations, labelled as C₁ and C₂, were installed in summer 2021 on either side of the north tongue of Belvedere Glacier (Fig. 1.1). The harsh glacier environment with steep and unstable moraines, often subject to rockfall due to glacier retreat, constrained the camera installation location at ~230 m (camera C₁) and ~350 m (camera C₂) from the terminal ice cliff, with a strongly convergent pose. Different lenses

Table 4.1: Summary of the characteristics of the two cameras. Fields marked with * are computed considering the distance between each camera and the ice cliff.

	C ₁	C ₂
Camera	Canon Eos 1200D	Canon Eos 1200D
Sensor	APS-C	APS-C
Pixel size	3.7 μ m	3.7 μ m
Image	6000 \times 4000 px	6000 \times 4000 px
Lens	Canon EF 24mm f/2.8 IS USM	Canon EF 35mm f/2 IS USM
Distance*	230 m	350 m
Average GSD*	3.5 cm px ⁻¹	3.5 cm px ⁻¹

were used for the two cameras to achieve the same image scale in correspondence of the glacier tongue: C₁ was equipped with a 24 mm lens, while a 35 mm lens was used for C₂.

The baseline between the two cameras of ~ 261 m ensured a good viewing geometry because of the large parallax between corresponding points. However, the baseline comparable to the camera-object distance (base-height ratio close to 1, Tab. 4.1) led to complex affinity-like distortions and occlusions between corresponding areas in the two images (?). Additionally, C₁ was positioned at a lower viewpoint compared to C₂, due to site geometry constraints. Therefore, camera C₁ provides a limited view that primarily encompasses the frontal ice cliff, but does not capture the glacier surface, which is only visible from camera C₂.

The stereoscopic system was operating from August 2021 up to December 2022, when it was temporarily unmounted for ordinary maintenance, and finally mounted again in June 2023. During the operational period, the system was programmed to acquire two images per day, but only one image per day was used for the multitemporal processing. Only daily images taken during the snow-free period between 01/05/2022 and 13/11/2022 were considered. In this period, the glacier is experiencing the most significant changes, flow velocity and ablation rates. On the other hand, during winter and spring seasons, the glacier was covered by snow, making it difficult to extract relevant information from optical images for tasks such as 3D reconstruction and surface velocity estimation.

The low-cost stereoscopic system for continuous monitoring is composed of two independent units, each housing an off-the-shelves DSLR camera. Each unit consists in an autonomous monitoring station that provides power supply, internet connectivity, timing and scheduling of image acquisition, and protection from the harsh environment. The station was designed and built adapting to the alpine environment an existing open-source model developed by Greig Sheridan and published on GitHub¹. A key aspect of the project was

¹Greig Sheridan' Intervalometer repository: <https://github.com/greiginsydney/Intervalometer>

to ensure easy assembly and realization of the system to guarantee future replication or improvement by non-experts. In the following, we describe in detail the services and the nominal performances provided by our system that make it worth consideration for applications in different monitoring contexts. Refer to Fig. 4.2 for a descriptive schematic of the whole system showing the components selected for the Belvedere Glacier case study. The choice of the camera and optics is discussed in Section XX, as these components are dependent on the domain of use of the stereoscopic system.

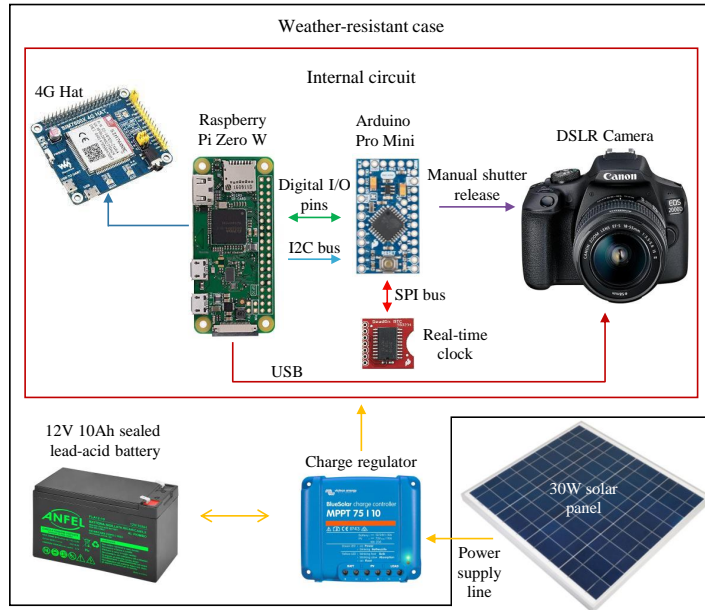


Figure 4.2: Scheme of the proposed acquisition system configuration for a single monitoring station. Arrows indicate the direction of signal initiation. Image adapted from Greig Sheridan's repository.

4.2.1 POWER SUPPLY

Each monitoring unit has its autonomous power supply line (yellow arrows in Figure 4.2) provided by a solar panel combined with a sealed lead-acid battery. An MPPT (Maximum Power Point Tracker) charge regulator directly connects with the unit's internal circuit, providing a regular current supply to the battery and the load and exploiting all the power generated by the panel. This regulator prevents any excess current that may damage the connected device, thus increasing the reliability of the system. Its battery life-saving algorithm modulates the load disconnection level so that a nearly 100% recharge is achieved about once every week and, in case of battery discharging, the whole system is switched off until 100% recharge of the battery is achieved. The whole

monitoring system is designed to minimise power consumption, e.g., by powering off devices responsible for the highest power consumption when not needed. An estimation of the system's energy consumption guided the choice of the components of the power supply line. Specifically, the battery and the associated panel must be accurately dimensioned for the system's purpose. To this end, the Photovoltaic Geographical Information System (PVGIS) (?), a tool provided by the European Commission, was used. PVGIS can estimate the performance of off-grid photovoltaic systems according to the installation site and it is supported by a database and algorithms for calculating solar radiation. Tuning the parameters for the Belvedere Glacier location and the system consumption, we ended up with the specifications of solar panel power of 30 W and battery voltage of 12 V and capacity of 10 Ah. Some compromises were made, accepting that the system would not be sufficiently powered in the months with lowest solar radiation (November, December, January, and February). [further details on PVGIS simulations for the Belvedere Glacier case study](#) are given.

4.2.2 SYSTEM CONTROL AND SCHEDULING

The internal electronic circuit (red box in Figure 4.2) of the monitoring unit is the only load connected to the power supply and is responsible for all the system's control and scheduling functionalities. Its components are a real-time clock (number 3 in Figure 4.3) with a 12 mm coin-cell backup battery, an Arduino microcontroller (Pro Mini 328 3.3V 8MHz, number 4 in Figure 4.3), a Raspberry Pi Zero W with 128 GB SD memory card (number 6 in Figure 4.3), and minor elements for connections, isolation (capacitors and optoisolators numbers 1 and 5 in Figure 4.3), and voltage regulations (numbers 2 in Figure 4.3). The circuit was realized manually by soldering wires and components on a stripboard (see Figure 4.3).

The Arduino communicates through an SPI (Serial Peripheral Interface) bus with an accurate real-time clock to schedule its actions: waking the camera, firing the shutter to take a photo, and turning on/off the Raspberry. The Raspberry is able to access the camera images and transfer them to a remote server via internet connectivity. A large storage memory is added to the unit to save photos before remote transferring. The Raspberry also provides a web-based, user-friendly interface (Figure 4.4) to configure and monitor the system remotely (?). An I₂C (Inter Integrated Circuit) bus and digital pin connections enable higher-level communication between these two boards. Among the minor components, we mention the role of the three voltage regulators. They allow each unit to be powered at the appropriate voltage and current: starting from the 12 V in input, one delivers 3.3 V and 500 mA to the Arduino, one 5 V and 2.5 A to the Raspberry and its hat, and the other 7.5 V and 2.4 A to the camera. The Arduino controls the 5V regulator of the Raspberry to reduce quiescent power consumption when the Raspberry board is off.

Acquisition of a defined number of images, camera triggering and timing, and sending of images to a

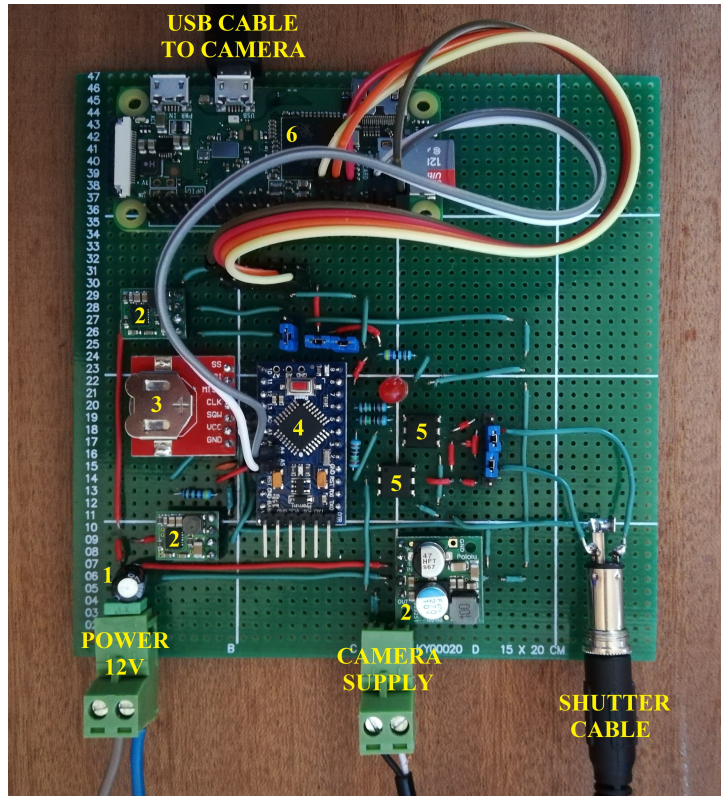


Figure 4.3: Stripboard on which are soldered the main components of the internal circuit: capacitors (1), voltage regulators (2), real-time clock with coin-cell battery (3), Arduino Pro Mini (4), optoisolators (5), and Raspberry Pi Zero W (6).

remote server can be scheduled thanks to adequate programming of a cyclic executive program in C++ for Arduino and of services executing automatically Python scripts for the Raspberry. All the monitoring station activities can be remotely scheduled from the terminal or a user-friendly web interface (?). This useful feature allows one to change the settings and check the behaviour of the system, avoiding the need for manual intervention. The Raspberry uses the gPhoto2, a Python-based protocol developed to specifically interact with popular cameras' firmware, to communicate with the camera and access the new photos. The web-based interface service is based on NGINX and Gunicorn, open-source software for web servers. The interface (Figure 4.4) consists of a web page accessible with credentials and provides a summary of the system state and the exact time of the last operations (time of the last shot and the last upload of images), temperatures of the components, previews of the last images, buttons to wake up the camera, take a preview photo and schedule the system routine (time and number of photo acquisition, wake-up time of the Raspberry) and some camera settings.

All the components were chosen because of their low power consumption and their inter-compatibility.

Figure 4.4: Example of some of the pages of the web-based interface to remotely control the monitoring units.

The circuit is robust against power losses due to battery discharging and is able to auto-recover when power is regained. A low energy consumption policy is also followed in selecting the scheduling. The camera is switched on only during the data capture activity. The Raspberry is switched on only once per day when the connection with the remote server and image transfer is scheduled.

4.2.3 CONNECTIVITY

Internet connectivity is crucial to transfer images and to control the units remotely. To this end, the Raspberry is equipped with the SIM7600E-H 4G hat by Waveshare. The module supports 4G/3G/2G communication via a SIM card. Raspberry and hat operations are the most expensive in terms of power consumption. For this reason, the board is switched on only once a day for a limited period of time, which is kept adequately low to be sustainable for the system power supply but still sufficient for transferring new images to the server. We adopted IoT (Internet of Things) SIM cards provided by the multi-operator service Emnify (?), as it offers the ability to connect to the best-quality cellular network available and includes flexible and customizable data plans. Remote access to the devices is allowed by a VPN (Virtual Private Network). The service costs €33 per month for a data plan with 6 GB.

4.2.4 CASE AND PROTECTION

The majority of the components need to be protected. Therefore, a solid and compact case that allows keeping all the parts (with the exception of the solar panel) in the same location is desirable for the functioning of the system and for convenient transportation, installation and maintenance. The case should also satisfy the thermal insulation requirements according to each component's working temperature range. The case should also be waterproof and robust against different and harsh weather conditions but, at the same time, provide access for connecting the solar panel and taking pictures. Our choice was an HPRC 2250 lightweight, waterproof resin case with internal insulating foam. The foam was found to be useful in enhancing the temperature seal and stabilising the location of some components, preventing unwanted movements. Holes were drilled in the case: one sealed with a UV filter of 82 mm to allow the camera to take shots, two others to give access to the solar panel wires, and others to fix the system to a tripod. The internal case dimensions (236x182x155 mm) posed a significant challenge in accommodating all the components inside. In particular, the camera lens dimensions were constrained by space availability.

4.2.5 GENERAL PERFORMANCES

The system was subject to several tests before being used in its final application at the Belvedere glacier site. During these tests, the system proved to be autonomous, robust to sudden shutdowns, cold-resistant, water-resistant and self-sufficient for a prolonged period of time with no direct sunlight on the solar panels. Specifically, in the absence of sunlight, the battery is able to power the system for about nine days before it is completely discharged. Battery voltage and temperatures of components were monitored, simulating the absence of solar radiation and low environmental temperatures. See Figure 4.5 for the performances of the system during these tests.

4.2.6 CAMERA AND LENSES

The choice of the DSLR camera and of the optics can be considered application-dependent. Therefore specifications regarding these components are reported in reference to the Belvedere glacier case study. Each monitoring station was equipped with a DSLR camera Canon EOS 2000D, with 24.1 MP CMOS APS-C sensor. This model was chosen because of the limited costs, the high image resolution and its compactness, as it must fit inside the case. Additionally, another fundamental requirement was camera compatibility with the gPhoto2 software. In the installation inside the system case, the traditional rechargeable battery was replaced by a special battery ("fake battery") equipped with a power supply cable, which provides a voltage of 7.5 V from the

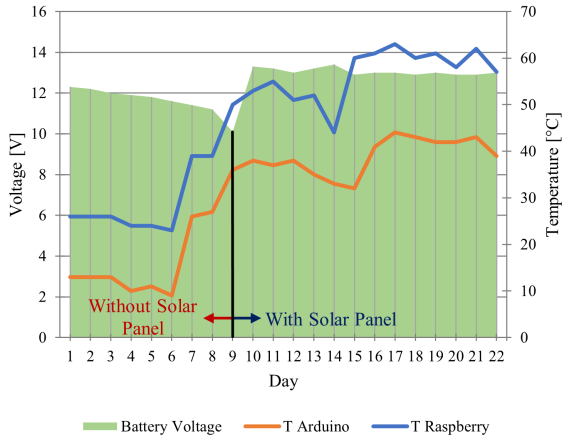


Figure 4.5: Battery voltage and temperature of boards with and without the solar panel during a period of tests. Starting from a fully charged condition, the system was kept without solar panel at around 2 °C for the first six days. After nine days, the battery was fully discharged and the system was reconnected to the panel and exposed to solar radiation.

circuit. The camera is attached to a sliding plate able to vary, with a limited range, and then fix the position of the camera on the longitudinal axis. Screws fix the camera to the plate and the plate to the case.

The two stations were installed respectively at ~ 180 m and ~ 340 m distance to the glacier terminus (see Figure 4.1), avoiding the steep moraines of the glacier, often prone to collapses and landslides. Therefore, a wide baseline of ~ 260 m occurs between the two sensors. The final positioning of the two cameras was decisive in the choice of optics. In fact, to ensure comparable Ground Sample Distance (GSD) of the images ($\sim 3 \text{ cm px}^{-1}$), lenses with different focal lengths were employed. In particular, a Canon EF 24 mm f/2.8 IS USM and a Canon EF 35 mm f/2 IS USM were used respectively for Camera 1 (stream-wise right) and Camera 2 (stream-wise left).

4.2.7 CAMERA INSTALLATION

Monumentation of the two cameras at the Belvedere Glacier site was achieved by choosing two large stable rocks along the moraines. Each camera is supported by an aluminium topographic tripod system anchored with steel dowels and cables to the rocks (Figure 4.6b). A central steel tie rod keeps the system in a fixed position. The choice of an agile monumentation was aimed at having a system that can be rather easily assembled on site (and also disassembled, if needed), also in a harsh environment, with limited costs and time. To install the cameras, in fact, all the equipment was carried in backpacks along the moraines, sometimes without a marked walking path (e.g., in the case of the stream-wise left camera). As a drawback, the analysis of the acquired photos revealed a non-optimal stabilization of the two cameras. In fact, small rotations, especially around the vertical axis, and

vibrations, mostly induced by the wind, were experienced. Though, a perfectly stable monummentation in a mountain environment is hardly achievable. Therefore, it is not possible to assume the camera orientation as stable a priori, but camera orientation must be estimated based on some Ground Control Points (GCPs) located on the ground in stable areas.

It is worth mentioning the performances of the system in terms of costs: our monitoring system can be fully reproduced with an average cost of €2000 per station (November 2023), including camera (€400), lens (€500) and material for the on-site installation (€150). In comparison, commercial time-lapse cameras are expensive (e.g., PhotoSentinel² cameras cost more than \$5,000.00) and hardly customizable. The final prototype of the monitoring station is shown in Figure 4.6.



Figure 4.6: (a) Picture of the monitoring unit prototype installed for tests at the Belvedere Glacier site. (b) Picture of the final monummentation of the camera installed on the stream-wise right moraine. **TODO: change picture with the final installation**

²PhotoSentinel: <https://photosentinel.com/> (accessed on 15/11/23)

4.3 DATASETS

4.3.1 STEREOSCOPIC IMAGE SEQUENCES

During the snow-free study period (from 1/05/2022 to 13/11/2022), both camera C₁ and camera C₂ were able to acquire images every day, for a total of 197 images. However, 39 images were discarded due to bad weather conditions, such as rain, low clouds, or fog, resulting in 158 days with valid data for stereo and monoscopic processing.

TODO: write about the images sequence 2022 and 2023

4.3.2 UAV SURVEYS

Two UAV flights, spaced by a 10-days interval, were conducted in summer 2022 to acquire ground truth data for assessing the proposed methodology. The first UAV flight, labelled as UAV-A, was carried out on 28/07/2022 with a DJI Matrice 300 RTK quadcopter and a DJI Zenmuse P1 camera with a 35 mm lens. During the survey, 436 images were captured, encompassing both nadiral and oblique perspectives. Additionally, 19 Ground Control Points (GCPs) were measured using a combination of a total station and Differential GPS (DGPS), employing a topographic-grade GNSS receiver. The GCPs included both artificial targets and natural features. During the flight, the UAV was equipped with an on-board RTK GNSS receiver, enabling the acquisition of camera projection centers with decimetric accuracy. The photogrammetric block (Fig. 4.7a) was processed with the commercial software package Agisoft Metashape (?) by using 14 GCPs and 5 Check Points (CPs) to evaluate the block accuracy. The global RMSE evaluated on the CPs was equal to 4.0 cm.

The second UAV flight, UAV-B, was carried out on 05/08/2022 with a DJI Phantom 4 RTK, focusing on a smaller portion of the northern lobe of the Belvedere Glacier. However, due to technical constraints, *moving* GCPs located inside the glacier body were not measured again. Therefore, only the fixed targets located outside the glacier were employed. Among these, 8 targets were designated as GCPs, while the remaining 4 were used as CPs. The photogrammetric block encompassed 428 nadiral and oblique images, which were processed using Agisoft Metashape (Fig. 4.7b). A global RMSE of 7.5 cm was obtained on the 4 CPs.

4.3.3 METEOROLOGICAL MONITORING STATION

To analyze the correlation between the Belvedere Glacier dynamics and external environmental variables, data measured from an Automatic Weather Station (AWS) located close to the Zamboni Zappa Hut were used. The AWS is located at an altitude of 2075 m a.s.l. and at a distance of 2 km from the area of study. In our study,

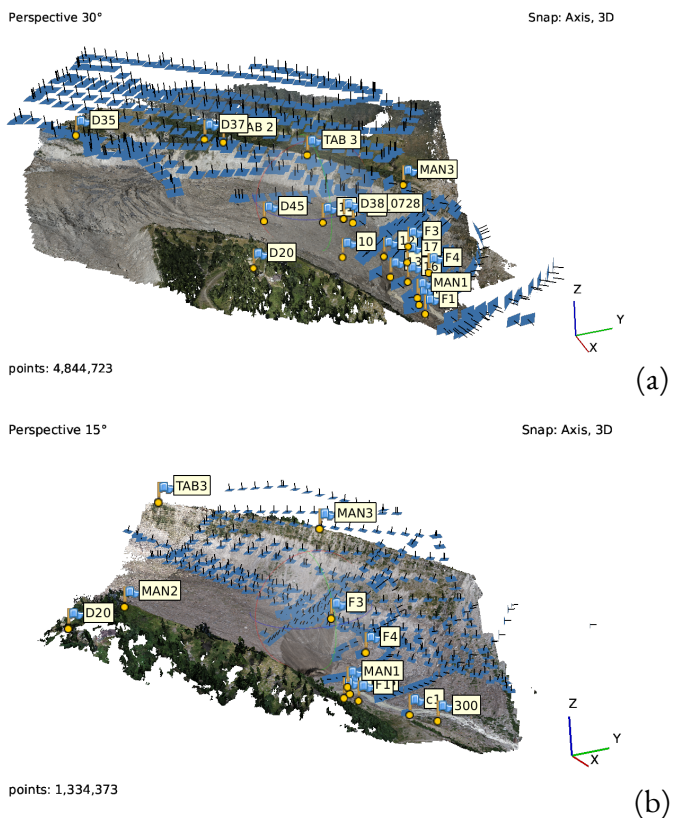


Figure 4.7: (a) UAV-A block and (b) UAV-B block processed with Agisoft Metashape. The flags represent the targets used either as GCPs in the BA or as CPs to evaluate the quality of the photogrammetric block.

we analyzed mean daily values of air temperature, precipitation and incoming solar radiation from 01/05/22 to 15/11/22.

4.4 METHODOLOGY

This chapter outlines the methodology developed to monitor the evolution of the Belvedere Glacier northern lobe. The daily images were processed using a framework consisting of two parallel processing chains (Fig. 4.8): (i) a photogrammetric-based stereoscopic approach; (ii) a DIC-based monoscopic approach. The daily stereo pairs were used to generate 3D models of the glacier terminus, enabling the estimation of ice volume loss on a daily basis by computing point cloud differences along the main flow direction. However, due to limited overlapping views of the two cameras, the stereoscopic approach primarily provides a 3D reconstruction of the terminal ice cliff (dashed-blue area in Fig. 1.1b). Consequently, deriving the 3D surface velocity field of the glacier solely from photogrammetry was not feasible. The image sequence captured by camera C₂, offering a higher viewpoint and broader coverage of the glacier surface, was employed to determine the glacier's surface velocity over a larger area of the north lobe of the Belvedere Glacier (dashed-green area in Fig. 1.1b).

4.4.1 IMAGE SELECTION

Once the acquired images have been received from the monitoring system, an automatic selection of the images was performed to exclude the ones acquired in rainy, foggy, or poor lighting conditions. This selection was based on the analysis of images median entropy (?): the images with a low value over the entire image were rejected. Additionally, a visual inspection was performed on the entire image dataset. The inspection had the following objectives: (i) selecting only one image per day; (ii) rejecting poor quality images that were not automatically rejected, and images in which the fixed targets placed along the moraines were not visible; (iii) detecting of sudden changes in the morphology of the glacier terminus (e.g., icefall).

4.4.2 CAMERA CALIBRATION

Each camera was mounted with all its electronics inside a waterproof case and protected by a neutral filter that was glued to the case and fixed in front of the cameras. Since the filter introduced additional distortion, the cameras need to be calibrated inside the boxes to reproduce the final setup. Therefore, a two-step approach was taken: first, a 120 cm x 70 cm calibration board with a checkerboard printed on it was used to estimate an initial set of parameters for the interior orientation (?). To this end, the cameras were mounted on tripods inside their cases while the calibration board was moved and rotated in front of the camera to simulate a convergent

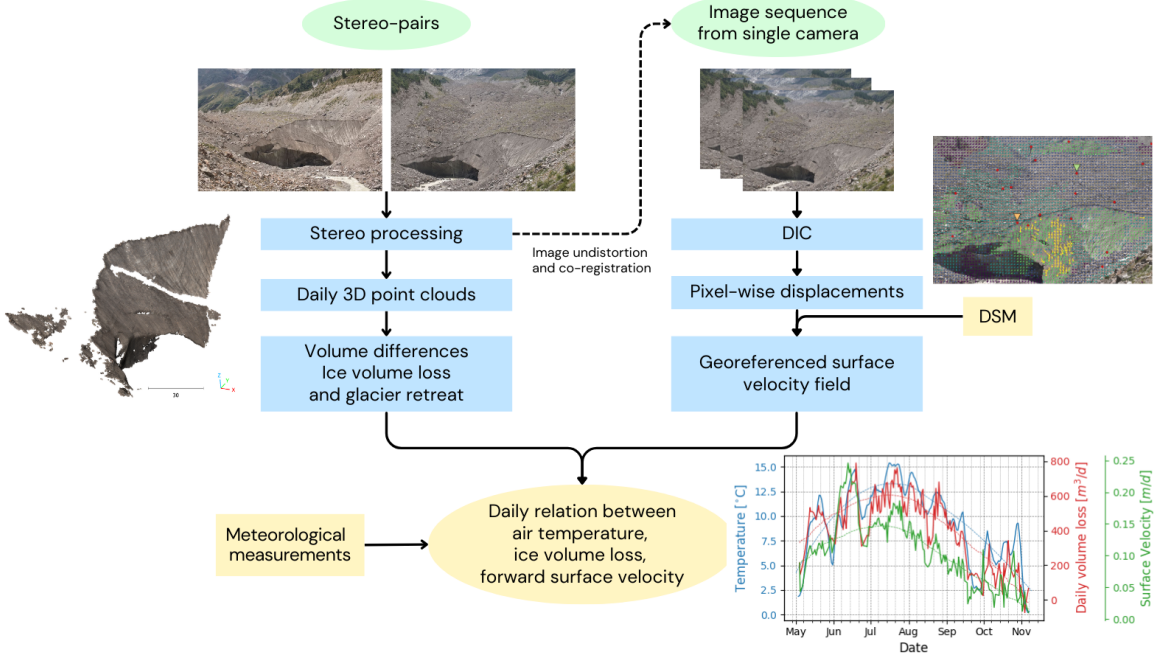


Figure 4.8: General workflow with two parallel processing chains involving stereoscopic reconstruction of terminal ice cliff from stereo-pairs of images to derive ice volume losses at the glacier terminus and glacier retreat and monoscopic digital-image correlation to derive surface velocities.

hemispheric acquisition. For each camera, about 30 images were collected and processed in Agisoft Metashape to obtain a first estimate of the interior orientation. However, the average camera-to-panel distance was much smaller than the actual camera-to-glacier distance. Therefore, a refinement of the calibration was performed in-situ by incorporating the stereo pair acquired by the cameras on 28/07/22, within the UAV-A block, carried out on the same day. This block was processed with Agisoft Metashape to refine the interior camera orientation of the stereo cameras, aided by the increased robustness of the block given by the additional matches between the two images taken by camera C₁ and C₂ and the UAV.

An additional challenge was represented by camera interior orientation stability over time. From experimental evidence, the interior orientation parameter that suffered the most because of temperature variations that occurred in mountain environment was the camera principal distance (?), while the other parameters remained more stable during time. To mitigate the impact of temperature-induced variations, it was crucial to incorporate camera self-calibration during the stereoscopic processing at each epoch to refine the pre-calibrated principal distance, following the procedure detailed in Sec. 4.4.2.

4.4.3 CAMERA STABILITY AND GCPs

Since the two cameras were mounted on topographic tripods, the stability of the cameras was not perfectly guaranteed. In particular, the two cameras experienced small vibrations around their pivots due to wind gusts. On the other hand, the position of the cameras was constrained by topographic heads that kept the position of the camera center constant to the centimeter level. Therefore, the baseline of the cameras can be reasonably considered as constant, with a value of 261.55 m. On the other hand, camera angular vibrations implied that the relative orientation of the cameras must be estimated at each epoch. Moreover, to fix the world reference system over time, absolute orientation of the stereo model was required. To this end, the position of the cameras was measured in-situ using a topography-grade GNSS receiver in RTK. In addition, four GCPs were materialized with plastic targets, anchored to stable rocks in front of the terminal ice cliff and along the streamwise left moraine (Fig. 1.1a). While the minimum requirement to estimate a Helmert transformation would have been just the two cameras' location and one GCP, having a redundant number of GCPs overcomes the possibility that on some days not all GCPs were clearly visible in the images due to low clouds or fog. Additionally, GCPs can be included into the BA to refine the cameras' interior orientation, and in particular the camera's focal length.

As the cameras are subjected to slight rotations, the image coordinates of the GCPs' projections must be detected at each epoch. To this end, a feature tracking routine was developed based on the ImGRAFT TemplateMatch method (?), enabling the detection of a template defined on a reference image within a target image through DIC. The routine utilized the orientation correlation algorithm (?), providing increased robustness against illumination changes and achieving sub-pixel accuracy (??).

5

Results

LOREM IPSUM DOLOR SIT AMET, consectetur adipiscing elit. Morbi commodo, ipsum sed pharetra gravida, orci magna rhoncus neque, id pulvinar odio lorem non turpis. Nullam sit amet enim. Suspendisse id velit vitae ligula volutpat condimentum. Aliquam erat volutpat. Sed quis velit. Nulla facilisi. Nulla libero. Vivamus pharetra posuere sapien. Nam consectetur. Sed aliquam, nunc eget euismod ullamcorper, lectus nunc ullamcorper orci, fermentum bibendum enim nibh eget ipsum. Donec porttitor ligula eu dolor. Maecenas vitae nulla consequat libero cursus venenatis. Nam magna enim, accumsan eu, blandit sed, blandit a, eros.

6

Discussion

LOREM IPSUM DOLOR SIT AMET, consectetur adipiscing elit. Morbi commodo, ipsum sed pharetra gravida, orci magna rhoncus neque, id pulvinar odio lorem non turpis. Nullam sit amet enim. Suspendisse id velit vitae ligula volutpat condimentum. Aliquam erat volutpat. Sed quis velit. Nulla facilisi. Nulla libero. Vivamus pharetra posuere sapien. Nam consectetur. Sed aliquam, nunc eget euismod ullamcorper, lectus nunc ullamcorper orci, fermentum bibendum enim nibh eget ipsum. Donec porttitor ligula eu dolor. Maecenas vitae nulla consequat libero cursus venenatis. Nam magna enim, accumsan eu, blandit sed, blandit a, eros.

7

Conclusion

Lorem ipsum dolor sit amet, consectetuer adipiscing elit. Morbi commodo, ipsum sed pharetra gravida, orci magna rhoncus neque, id pulvinar odio lorem non turpis. Nullam sit amet enim. Suspendisse id velit vitae ligula volutpat condimentum. Aliquam erat volutpat. Sed quis velit. Nulla facilisi. Nulla libero. Vivamus pharetra posuere sapien. Nam consectetuer. Sed aliquam, nunc eget euismod ullamcorper, lectus nunc ullamcorper orci, fermentum bibendum enim nibh eget ipsum. Donec porttitor ligula eu dolor. Maecenas vitae nulla consequat libero cursus venenatis. Nam magna enim, accumsan eu, blandit sed, blandit a, eros.

A

Some extra stuff

Lorem ipsum dolor sit amet, consectetur adipiscing elit. Morbi commodo, ipsum sed pharetra gravida, orci magna rhoncus neque, id pulvinar odio lorem non turpis. Nullam sit amet enim. Suspendisse id velit vitae ligula volutpat condimentum. Aliquam erat volutpat. Sed quis velit. Nulla facilisi. Nulla libero. Vivamus pharetra posuere sapien. Nam consectetur. Sed aliquam, nunc eget euismod ullamcorper, lectus nunc ullamcorper orci, fermentum bibendum enim nibh eget ipsum. Donec porttitor ligula eu dolor. Maecenas vitae nulla consequat libero cursus venenatis. Nam magna enim, accumsan eu, blandit sed, blandit a, eros.